



Topography of epithelial–mesenchymal plasticity

Francesc Font-Clos^a, Stefano Zapperi^{a,b}, and Caterina A. M. La Porta^{c,1}

^aCenter for Complexity and Biosystems, Department of Physics, University of Milan, 20133 Milano, Italy; ^bConsiglio Nazionale delle Ricerche, Istituto di Chimica della Materia Condensata e di Tecnologie per l'Energia, 20125 Milano, Italy; and ^cCenter for Complexity and Biosystems, Department of Environmental Science and Policy, University of Milan, 20133 Milano, Italy

Edited by José N. Onuchic, Rice University, Houston, TX, and approved April 27, 2018 (received for review December 29, 2017)

The transition between epithelial and mesenchymal states has fundamental importance for embryonic development, stem cell reprogramming, and cancer progression. Here, we construct a topographic map underlying epithelial–mesenchymal transitions using a combination of numerical simulations of a Boolean network model and the analysis of bulk and single-cell gene expression data. The map reveals a multitude of metastable hybrid phenotypic states, separating stable epithelial and mesenchymal states, and is reminiscent of the free energy measured in glassy materials and disordered solids. Our work not only elucidates the nature of hybrid mesenchymal/epithelial states but also provides a general strategy to construct a topographic representation of phenotypic plasticity from gene expression data using statistical physics methods.

epithelial–mesenchymal transition | epigenetic landscape | Boolean networks

Epithelial (E) cells can transdifferentiate into mesenchymal (M) cells and vice versa under a cohort of transcription factors, including the Snail and Zeb families (1). The E to M transition (EMT), associated with the loss of cell–cell adhesion and the gain of invasive traits, is considered to be a hallmark of plasticity within a stem cell population and is particularly relevant for tumors. For this reason, a great effort has been devoted in the past to identify the critical biological functions regulating the EMT and its reverse, the M to E transition (MET). Almost 80% of human malignancies originate from E tissues, and a transition toward an M phenotype is usually associated with more aggressive potential (2–5). Emerging evidence shows that the EMT is a multiple-step process where cells express a mix of markers, both characteristic of E and M cells (6–8). These recent results are blurring the rigid distinction between E and M phenotypes, indicating that cancer cells can acquire hybrid E/M phenotypes, combining invasive capabilities with intracellular adhesion (9, 10), becoming extremely aggressive and associated with poor patient outcome (11, 12).

According to an old and influential metaphor from Waddington (13), the cell phenotype is analogous to a marble rolling over an epigenetic landscape, and phenotypic plasticity corresponds to the marble crossing a hill separating different valleys. This landscape should correspond to the attractors of the kinetics of gene regulatory networks (14–21) and be encoded in gene expression data (22, 23). Here, we combine numerical simulations of a large Boolean model for the EMT–MET network with the analysis of a wide set of bulk and single-cell gene expression data to reconstruct the topography underlying E/M plasticity. Genetic circuits regulating the EMT have been widely investigated theoretically, with models ranging from simple switches composed of a few genes (24) to large complex networks requiring extensive numerical simulations, in both discrete (25, 26) and continuous time (27). Some of these models have provided insights into particular EMTs, generating hypotheses that have later been experimentally tested (26). We show how these models can be used to rationalize and classify genetic drivers of the EMT and clarify the nature of hybrid E/M states guided by the Waddington picture (13).

Our results reveal that EMT/MET occurs across an extremely complex landscape characterized by a startling number of valleys and mountains organized according to a scale-free hierarchical statistical pattern. We observe a multitude of stable E/M

states separated by a series of progressively less stable and more hybrid states that are increasingly prone to phenotypic changes in response to external perturbations. Hence, EMTs and METs can take place in widely different locations and across multiple paths, in close analogy with nonequilibrium phase transitions in disordered solids (28, 29).

Model

To reconstruct the topographic landscape of E/M plasticity, we chose to build on the large Boolean network model previously used to investigate EMT in hepatocellular carcinoma (25, 26). Since the model as it stands is hardwired toward EMT and MET is completely suppressed, we added to the model a missing contribution from the LIF/KLF4 pathway, whose role for MET has been widely reported (30, 31) (see *SI Appendix*, Fig. S1, Dataset S1, and *SI Appendix* for details). In this way, we obtained a network of $N = 72$ nodes, whose state is defined by a string of binary variables $\{s_i\}$, determining if each gene/factor i is expressed/present ($s_i = 1$) or not ($s_i = -1$). Regulatory relations between two nodes i and j were encoded into a (nonsymmetric) matrix J_{ij} taking the value $J_{ij} = 1$ if j promotes i and $J_{ij} = -1$ when j inhibits i (see Dataset S2). The network nodes evolve asynchronously according to a simple majority rule, so that the node is set to $s_i = 1$ if the sum of its promoting interactions is larger than the sum of its inhibitory ones (see Fig. 14) (32). In case of ties, the node was not updated, keeping its present state (15). This evolution rule is the binary version of the half-functional rule recently proposed in ref. 27 to construct continuum kinetic reaction models from pathways and can be formally expressed as

$$s_i(t+1) = \text{sign} \left(\sum_j J_{ij} s_j(t) \right), \quad [1]$$

Significance

Cells can change their phenotype from epithelial to mesenchymal during development and in cancer progression, where this transition is often associated with metastasis and poor disease prognosis. Here we show this process involves the transit through a multitude of metastable hybrid phenotypes in a way that is similar to the driven dynamics of disordered materials. Our method shows that highly aggressive hybrid epithelial/mesenchymal cell phenotypes are located in metastable regions that can easily switch under external and internal perturbations. We propose a general mapping strategy that can be used for other pathways, providing a useful tool to visualize the ever increasing number of gene expression data obtained from single cells and tissues.

Author contributions: S.Z. and C.A.M.L.P. designed research; F.F.-C. performed research; F.F.-C. analyzed data; and F.F.-C., S.Z., and C.A.M.L.P. wrote the paper.

The authors declare no conflict of interest.

This article is a PNAS Direct Submission.

Published under the PNAS license.

¹To whom correspondence should be addressed. Email: caterina.laporta@unimi.it.

This article contains supporting information online at www.pnas.org/lookup/suppl/doi:10.1073/pnas.1722609115/-DCSupplemental.

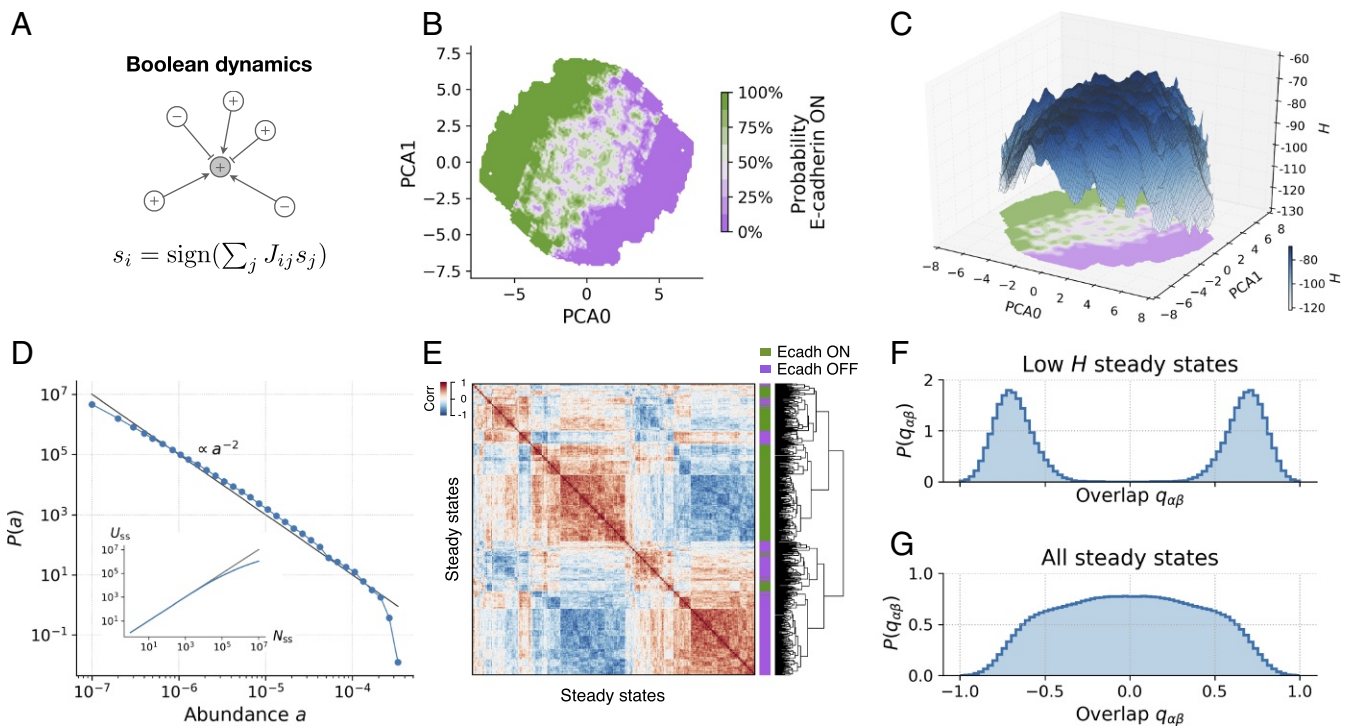


Fig. 1. The topography of E/M states displays a hierarchical complex structure. (A) Illustration of the Boolean update rule. The state of a node s_i depends on the state of its promoters ($J_{ij} = +1, \rightarrow$) and inhibitors ($J_{ij} = -1, \leftarrow$). (B) PCA projection of 10^6 steady states. Color corresponds to the ratio of steady states that express E-cadherin. The panel shows intricate patterns of transition between areas of high/low E-cadherin expression probability, colored in green/violet shades. (C) A 3D reconstruction of topography of EMT. The xy projection reproduces the data in B. The z axis corresponds to the value of H , showing that high- H states (colored in darker blue shades) coincide with the central transition area in B. (D) Distribution of steady-state abundances, computed from 10^7 steady states of the EMT model (blue symbols). The relative abundance a of a steady state is the fraction of times it is found, starting from random initial conditions. The black line of slope -2 is shown only as a guide to the eye. The *Inset* shows the number of distinct steady states U_{ss} as a function of the total number of steady states N_{ss} found in the simulations. (E) Clustering of steady states, computed using 500 steady states of the model. The heat map shows the correlation between steady states. Colors adjacent to the dendrogram mark the expression of E-cadherin (green) or lack of expression (violet). States expressing E-cadherin cluster together but display additional hierarchical organization. (F) Overlap distribution over the 20% of steady states with lowest H . A two-peak distribution marks the presence of two symmetric sets as in disordered magnets. (G) The broad overlap distribution over all steady states resembles the one observed in spin glasses.

which is the same equation used to simulate the zero-temperature dynamics in random ferromagnets (28) and spin glasses (29). (Modifications of the model that include local random fields and their relation to network reconstruction errors are discussed in *SI Appendix*. See also *SI Appendix*, Fig. S8.) Guided by the analogy with magnetic systems, we defined a pseudo-Hamiltonian $H = -\sum_{i,j} J_{ij} s_i s_j$. When interactions are strictly symmetric ($J_{ij} = J_{ji}$), the fixed points of Eq. 1 are local minima of H . This is not guaranteed in our case since the interaction matrix is not symmetric (33, 34). We can, however, still show that H is lowered under repeated application of the evolution rule in Eq. 1 (see *SI Appendix* for full derivations and *SI Appendix*, Fig. S9). Hence, H provides a measure of the stability of a network state, with low- H states being more stable than high- H states.

Results

Simulated E/M Topography Displays Fractal Features. A phenotypic landscape associated with our EMT/MET network can be reconstructed by performing a large number ($M_0 = 10^7$) of simulations, starting from random initial conditions until the network reaches a steady state where s_i does not change. (No limit cycles are found; see *SI Appendix* for details.) In this way, we find a large number of distinct steady states that can be projected into a two-dimensional map using principal component analysis (PCA). We classify these steady states according to the expression of E-cadherin (CDH1), which we use as a reporter of the E/M phenotype (see Fig. 1B). The E/M map reconstructed from the model shows a clear separation between E and M states, with a

boundary layer where E and M states coexist in very close proximity. A topographic representation of the stability of the states can be obtained by projecting H on the same two-dimensional map (Fig. 1C) showing that the boundary layer is more elevated with respect to pure E/M states, suggesting that those states are less stable. Furthermore, the map displays a very rough topography, with two main valleys separated by a large barrier populated by smaller and smaller valleys.

Given the sheer amount of distinct steady states (see Fig. 1D, *Inset*), we resorted to a statistical analysis and computed the probability distribution $P(a)$ of the relative abundances of the states, where a is the fraction of times we find a given state. Fig. 1D shows that $P(a)$ is a power law distribution, indicating that most of the states are very rarely found [when a is small, $P(a)$ is large], but few states are found multiple times [when a is large, $P(a)$ is small]. Alternative functional forms for $P(a)$ are discussed in *SI Appendix* and shown in *SI Appendix*, Fig. S10. The presence of a power law is a signature of a scale-free fractal organization of the map, as is also apparent by the correlation matrix of the states. Fig. 1E shows the presence of large correlated clusters subdivided into smaller and smaller clusters. In the physics of disordered systems, a hierarchical organization of the states is traditionally revealed by a broad distribution $P(q_{\alpha\beta})$ of states' overlap $q_{\alpha\beta} = \sum_i (s_i^\alpha s_i^\beta) / N$, measuring the similarity between two states $\{s_i^\alpha\}$ and $\{s_i^\beta\}$ (35). Hierarchical ground state structures have been observed in short-range Ising spin glasses (see refs. 36 and 37). When we restrict the sampling to low- H states, $P(q_{\alpha\beta})$ displays a two-peak structure, indicating the presence of

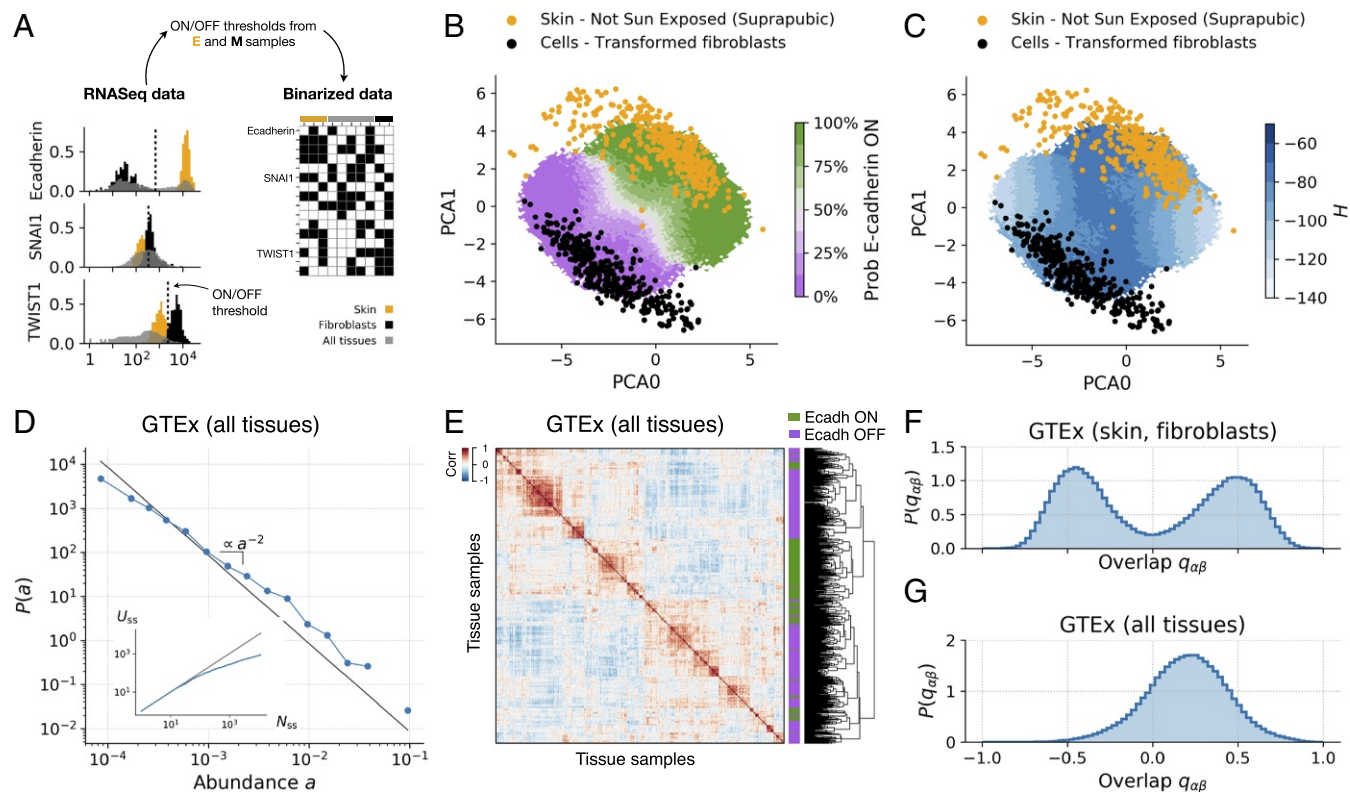


Fig. 3. Multitissue gene expression data display statistical features in agreement with simulations. (A) Illustration of the binarization process (see *Materials and Methods* for details). Gene-level expression data are casted into node-level binary data using binarization thresholds, computed using two reference samples (orange and black coloring). (B) Skin (orange) and fibroblast (black) samples from the GTEx project projected in PCA space. The E-cadherin expression probability in the model is shown with green (100%) to violet (0%) shades. Fibroblast samples tend to be in areas of very low E-cadherin expression probability. (C) Same as B but coloring the model steady states by average H . (D) Distribution of abundances, computed using all GTEx binarized samples and the 14 most relevant nodes (see *SI Appendix* and *SI Appendix*, Fig. S3 for details). (E) Clustering of 500 GTEx samples (all tissues), displaying a hierarchical structure qualitatively similar to that of the model (compare with Fig. 1E). (F) Overlap distribution over skin and fibroblast samples from the GTEx project (compare with Fig. 1F). (G) Overlap distribution over all GTEx samples (compare with Fig. 1G).

Fig. 3C). We used the same strategy to localize on the same topographic map the entire set of tissues present in the GTEx database (see *SI Appendix*, Figs. S4 and S5) and showed that they cover all of the available phase space. Assuming that the GTEx database contains an unbiased random sampling of all of the available states—which is a reasonable assumption given that the GTEx project provides multitissue gene expression data from healthy individuals only (41)—we analyzed the statistical properties of these states. As shown in Fig. 3D, the abundance distribution derived from GTEx data decays as a power law with an exponent that is very close to the one found numerically (compare with Fig. 1D and see *SI Appendix* and *SI Appendix*, Fig. S4 for technical details). Furthermore, clustering of the states showed a correlation matrix with hierarchical features that are in reasonable agreement with the prediction of the model (compare Fig. 3E with Fig. 1E). Finally, the overlap distribution displayed a two-peak structure when the statistics were restricted to fibroblasts and skin cells (Fig. 3F), while a single-peaked distribution was found when using all of the GTEx samples (Fig. 3G). This is in close agreement with the simulation results reported in Fig. 1 and confirms that experimental gene expression data give rise to a topographic landscape quantitatively similar to the one predicted by the model.

Tracing Bulk and Single-Cell RNA-Sequencing Trajectories Reveals the Nature of Hybrid E/M States. The topographic representation of E/M states derived above can be used to visualize and interpret RNA-sequencing (RNA-seq) data obtained while the cells are undergoing phenotypic transformations. We first consider the classical example of TGF- β -induced EMT in a human lung

adenocarcinoma cell line (42). Fig. 4A reports the trajectory of the states obtained from the bulk RNA-seq data recorded at different time points after TGF- β induction. As expected, the trajectory starts from the E region and crosses over to the M region of the map, as revealed by coloring the map according to the predicted expression of CDH1. Conversely, the trajectory obtained from RNA-seq data for DOX-induced MET during somatic cell reprogramming starts from the M valley and moves into the E valley of the landscape (30).

Our methodology is even more revealing when applied to single-cell RNA-seq (scRNA-seq) data, as shown in Fig. 4C, which reports the time course of the states obtained from scRNA-seq data undergoing EMT during embryonic to endoderm differentiation (43) [see also *SI Appendix*, Fig. S6 illustrating MET during fibroblast to cardiomyocyte reprogramming in single-cell and bulk samples (44)]. As time goes on, cells originally in the E region transition to the M region between 24 and 36 h. After this time, even though EMT is apparently completed, the kinetic evolution of the cell population does not stop, and the region occupied by single-cell states shrinks. If we color the map by the predicted expression of other markers, we observe that the evolution moves cells in a low-KLF4 region (Fig. 4C; see also *SI Appendix*, Fig. S7 for similar maps for other markers). Hence, when applied to scRNA-seq data, our method can reveal subtle features associated with phenotypic transformations.

This last point is best illustrated by analyzing recent data (6,000 single cells) obtained from 18 head and neck squamous cell carcinoma patients (45). The original analysis revealed the presence of an aggressive cancer cell population, associated with metastasis and poor prognosis, described as partial-EMT (pEMT) (45).

when the reference samples were of unequal size. The statistical significance of the binarization procedure was assessed with the Fisher's exact test. The EMT–MET model takes into account the localization of β -catenin by considering two separate nodes: one for β -catenin located in the nucleus, and one for β -catenin in the membrane. In gene-expression datasets, it is not possible to infer the localization of β -catenin looking only at the expression level of CTNNB1. To circumvent this issue, we considered β -catenin to be in the nucleus if its targets TCF/LEF were expressed, and in the membrane otherwise. If CTNNB1 was not expressed, the state of both nodes was set to -1 independently of the value of TCF/LEF.

Datasets. Data in Fig. 3 came from the GTEx project (41) and were downloaded from the GTEx portal (<https://gtexportal.org/home/datasets>) on October 12, 2017. We used samples labeled as “Cells–Transformed Fibroblasts” and “Skin–Not Sun Exposed (Suprapubic)” as reference samples for binarization. The PCA basis presented in Fig. 3 B and C was computed using all GTEx samples. All nodes were included in this analysis. The TGB- β -induced EMT data presented in Fig. 4A were downloaded from the Gene Expression Omnibus (accession no. GSE17708) (42) on September 25, 2017. We used $T = 0.5$, 1 h and $T = 24$, 72 h as reference samples for binarization. A total of 29 nodes with a binarization P value below 0.05 were included in the analysis. We used 10^7 steady states from the model, restricted to such nodes, to compute the PCA basis in Fig. 4A. Dox-induced MET data in Fig. 4B were downloaded from the Gene Expression Omnibus (accession no. GSE21757) (30), on October 2, 2017. We used $T = 0$ d and $T = 21$ d as

reference samples for binarization. With one single sample per time point, binarization P values could not be computed as explained above. As an alternative, we restricted the analysis to 47 nodes with a fold-change greater than or equal to 0.5. We used 10^7 steady states from the model, restricted to such nodes, to compute the PCA basis in Fig. 4B. Single-cell data of embryonic-to-endoderm differentiation presented in Fig. 4C were downloaded from the Gene Expression Omnibus (accession no. GSE75748) (43), on September 25, 2017. We used $T = 0$ h and $T = 96$ h as reference samples. Given the large number of samples, the PCA basis presented in Fig. 4C was computed using the experimental data. All nodes were included in the analysis. Head and neck cancer single-cell data presented in Fig. 4D and E were obtained from the Gene Expression Omnibus (accession no. GSE103322). We used E and fibroblast samples as reference samples for binarization. The PCA basis was fitted to the single-cell data using all nodes. The pEMT score was computed as the average expression of the 100 genes that constitute the pEMT program in ref. 45. Fibroblast-to-cardiomyocyte differentiation data in *SI Appendix, Fig. S6* were downloaded from the Gene Expression Omnibus [accession nos. GSE98570 (bulk data) and GSE98567 (single-cell data)] (44), on November 22, 2017. We used samples labeled as “control” and “reprogramming cells” as reference samples for single-cell data binarization and samples labeled as “D0” and “D14” for bulk data binarization. Single-cell data were used to fit the PCA basis presented in *SI Appendix, Fig. S7*.

ACKNOWLEDGMENTS. F.F.-C. and S.Z. are supported by European Research Council Advanced Grant 291002 SIZEEFFECTS.

- Ye X, Weinberg RA (2015) Epithelial-mesenchymal plasticity: A central regulator of cancer progression. *Trends Cell Biol* 25:675–686.
- Huber MA, Kraut N, Beug H (2005) Molecular requirements for epithelial-mesenchymal transition during tumor progression. *Curr Opin Cell Biol* 17:548–558.
- Rhim AD, et al. (2012) EMT and dissemination precede pancreatic tumor formation. *Cell* 148:349–361.
- Sarrió D, et al. (2008) Epithelial-mesenchymal transition in breast cancer relates to the basal-like phenotype. *Cancer Res* 68:989–997.
- Aleskandarany MA, et al. (2014) Epithelial mesenchymal transition in early invasive breast cancer: An immunohistochemical and reverse phase protein array study. *Breast Cancer Res Treat* 145:339–348.
- Bitterman P, Chun B, Kurman RJ (1990) The significance of epithelial differentiation in mixed mesodermal tumors of the uterus. A clinicopathologic and immunohistochemical study. *Am J Surg Pathol* 14:317–328.
- Haraguchi S, Fukuda Y, Sugisaki Y, Yamanaka N (1999) Pulmonary carcinosarcoma: Immunohistochemical and ultrastructural studies. *Pathol Int* 49:903–908.
- Paniz Mondolfi AE, et al. (2013) Primary cutaneous carcinosarcoma: Insights into its clonal origin and mutational pattern expression analysis through next-generation sequencing. *Hum Pathol* 44:2853–2860.
- Revenu C, Gilmour D (2009) Emt 2.0: Shaping epithelia through collective migration. *Curr Opin Genet Dev* 19:338–342.
- Yu M, et al. (2013) Circulating breast tumor cells exhibit dynamic changes in epithelial and mesenchymal composition. *Science* 339:580–584.
- Jolly MK, et al. (2016) Stability of the hybrid epithelial/mesenchymal phenotype. *Oncotarget* 7:27067–27084.
- George JT, Jolly MK, Xu S, Somarelli JA, Levine H (2017) Survival outcomes in cancer patients predicted by a partial EMT gene expression scoring metric. *Cancer Res* 77:6415–6428.
- Waddington C (1957) *The Strategy of the Genes* (Allen & Unwin, London).
- Kauffman SA (1969) Metabolic stability and epigenesis in randomly constructed genetic nets. *J Theor Biol* 22:437–467.
- Li F, Long T, Lu Y, Ouyang Q, Tang C (2004) The yeast cell-cycle network is robustly designed. *Proc Natl Acad Sci USA* 101:4781–4786.
- Huang S, Eichler G, Bar-Yam Y, Ingber DE (2005) Cell fates as high-dimensional attractor states of a complex gene regulatory network. *Phys Rev Lett* 94:128701.
- Huang S, Guo YP, May G, Enver T (2007) Bifurcation dynamics in lineage-commitment in bipotent progenitor cells. *Dev Biol* 305:695–713.
- Wang J, Xu L, Wang E, Huang S (2010) The potential landscape of genetic circuits imposes the arrow of time in stem cell differentiation. *Biophys J* 99:29–39.
- Wang J, Zhang K, Xu L, Wang E (2011) Quantifying the Waddington landscape and biological paths for development and differentiation. *Proc Natl Acad Sci USA* 108:8257–8262.
- Huang S (2012) The molecular and mathematical basis of Waddington's epigenetic landscape: A framework for post-Darwinian biology? *Bioessays* 34:149–157.
- Li C, Wang J (2013) Quantifying Waddington landscapes and paths of non-adiabatic cell fate decisions for differentiation, reprogramming and transdifferentiation. *J R Soc Interface* 10:20130787.
- Scialdone A, et al. (2016) Resolving early mesoderm diversification through single-cell expression profiling. *Nature* 535:289–293.
- Bargaje R, et al. (2017) Cell population structure prior to bifurcation predicts efficiency of directed differentiation in human induced pluripotent cells. *Proc Natl Acad Sci USA* 114(9):2271–2276.
- Jolly MK, et al. (2014) Towards elucidating the connection between epithelial-mesenchymal transitions and stemness. *J R Soc Interface* 11:20140962.
- Steinway SN, et al. (2014) Network modeling of TGF-beta signaling in hepatocellular carcinoma epithelial-to-mesenchymal transition reveals joint sonic hedgehog and wnt pathway activation. *Cancer Res* 74:5963–5977.
- Steinway SN, et al. (2015) Combinatorial interventions inhibit TGF-beta-driven epithelial-to-mesenchymal transition and support hybrid cellular phenotypes. *NPJ Syst Biol Appl* 1:15014.
- Huang B, et al. (2017) Interrogating the topological robustness of gene regulatory circuits by randomization. *PLoS Comput Biol* 13:e1005456.
- Sethna JP, et al. (1993) Hysteresis and hierarchies: Dynamics of disorder-driven first-order phase transformations. *Phys Rev Lett* 70:3347–3350.
- Pázmándi F, Zaránd G, Zimányi GT (1999) Self-organized criticality in the hysteresis of the Sherrington-Kirkpatrick model. *Phys Rev Lett* 83:1034–1037.
- Samavarchi-Tehrani P, et al. (2010) Functional genomics reveals a BMP-driven mesenchymal-to-epithelial transition in the initiation of somatic cell reprogramming. *Cell Stem Cell* 7:64–77.
- Li R, et al. (2010) A mesenchymal-to-epithelial transition initiates and is required for the nuclear reprogramming of mouse fibroblasts. *Cell Stem Cell* 7:51–63.
- Bornholdt S (2008) Boolean network models of cellular regulation: Prospects and limitations. *J R Soc Interface* 5(Suppl 1):S85–S94.
- Derrida B (1987) Dynamical phase transition in nonsymmetric spin glasses. *J Phys A Math Gen* 20:L721–L725.
- Gutfreund H, Reger JD, Young AP (1988) The nature of attractors in an asymmetric spin glass with deterministic dynamics. *J Phys A Math Gen* 21:2775–2797.
- Mezard M, Parisi G, Virasoro MA (1987) *Spin Glass Theory and Beyond* (World Scientific, Singapore).
- Hed G, Hartmann AK, Stauffer D, Domany E (2001) Spin domains generate hierarchical ground state structure in $J = +/-1$ spin glasses. *Phys Rev Lett* 86:3148–3151.
- Hed G, Young AP, Domany E (2004) Lack of ultrametricity in the low-temperature phase of three-dimensional Ising spin glasses. *Phys Rev Lett* 92:157201.
- Derrida B, Flyvbjerg H (1986) Multivalley structure in Kauffman's model: Analogy with spin glasses. *J Phys A Math Gen* 19:L1003–L1008.
- Miranda EN, Parga N (1988) Ultrametricity in the Kauffman model: A numerical test. *J Phys A Math Gen* 21:L357–L361.
- Bastolla U, Parisi G (1996) Closing probabilities in the Kauffman model: An annealed computation. *Physica D Nonlinear Phenomena* 98:1–25.
- Carithers LJ, et al. (2015) A novel approach to high-quality postmortem tissue procurement: The GTEx project. *Biopreservation and Biobanking* 13:311–319.
- Abnaof K, et al. (2014) Tgf-beta stimulation in human and murine cells reveals commonly affected biological processes and pathways at transcription level. *BMC Syst Biol* 8:55.
- Chu LF, et al. (2016) Single-cell RNA-seq reveals novel regulators of human embryonic stem cell differentiation to definitive endoderm. *Genome Biol* 17:173.
- Liu Z, et al. (2017) Single-cell transcriptomics reconstructs fate conversion from fibroblast to cardiomyocyte. *Nature* 551:100–104.
- Puram SV, et al. (2017) Single-cell transcriptomic analysis of primary and metastatic tumor ecosystems in head and neck cancer. *Cell* 171:1611–1624.e24.